Submonolayer and Monolayer Sn Adsorption and Diffusion Behavior on Oxidized Nb(100)

Sarah A. Willson, Rachael G. Farber, Ajinkya C. Hire, R. G. Hennig, and S. J. Sibener*

Read Online

ACCESS | Metrics & More | Article Recommendations

ABSTRACT: Current efforts to produce brighter beams of charged particles are focused on developing Nb_3Sn-coated superconducting radio frequency (SRF) cavities for use in superconducting accelerator facilities. The growth mechanisms driving the formation of Nb_3Sn films on preexisting Nb SRF cavities are not, however, fully understood. In order to understand the complex interplay between metallic Sn and the oxidized Nb surface leading to Nb_3Sn alloy formation, we have examined how the structural and chemical composition of an oxidized Nb(100) single crystal influences Sn adsorption and diffusion behavior at submonolayer and monolayer Sn coverages. Sn was deposited on an NbO surface and annealed at temperatures relevant to Nb_3Sn growth procedures before analysis via *in situ* scanning tunneling microscopy (STM). Experimental data, along with supporting simulated STM and calculated binding energies obtained using density functional theory, revealed the influence of Sn coverage and annealing temperatures on thermodynamic and kinetically driven diffusion pathways, preferred binding sites, novel Sn adlayer structures, and how the underlying NbO substrate evolves to accommodate Sn diffusion. This newly realized understanding of the interfacial chemical interactions between adsorbed Sn and the Nb surface sites is essential to develop predictive growth models for Nb_3Sn films for use in future SRF cavities.
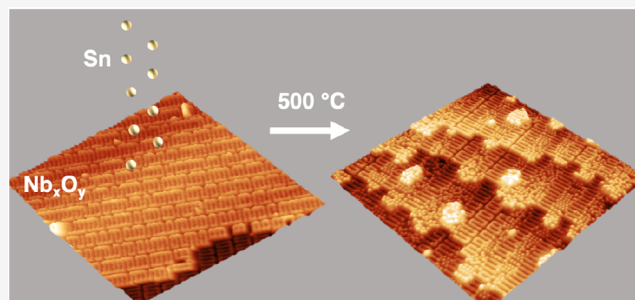
INTRODUCTION

Modern superconducting accelerator facilities rely on Nb superconducting radio frequency (SRF) cavities to effectively generate beams necessary for high-energy applications including X-ray free electron (FEL) laser radiation. Nb is the current standard for such SRF cavities due to several intrinsic material properties including its critical temperature (T_c) of ~9.8 K, the highest elemental T_c, and its high quality factor (Q) at operating temperatures of ~2 K.[1−3] The associated cryogenic infrastructure, energy consumption, and operating costs of Nb SRF cavities do, however, limit access to superconducting technology.

To increase the accessibility of superconducting science and technology, significant effort has been dedicated to identifying superconducting materials that can operate above ~2 K with comparable Q to Nb SRF cavities. One of the most promising materials identified is Nb_3Sn, an A15 alloy with a T_c of ~18 K that has been shown to be capable of operating at 4 K with Q comparable to Nb SRF cavities operating at ~2 K.[4−7] This increase in operating temperature significantly reduces the size and cost of cryogenic infrastructure, with recent work showing the successful operation of Nb_3Sn SRF cavities cooled via cryocooler conduction.[8] Despite these technological advancements, current Nb_3Sn SRF cavities are not operating at predicted metrics.[9] Recent work has associated SRF performance with micron-scale Nb_3Sn film morphological features such as inhomogeneous Sn concentration gradients within the SRF cavity.[10−12]

While Nb SRF cavities can be mechanically shaped into the desired cavity shape,[1,2] Nb_3Sn is extremely brittle and cannot withstand the physical manipulation needed to form SRF cavities. Instead, Nb_3Sn SRF cavities are fabricated, typically through the Wuppertal process, in which a Nb_3Sn film is grown on a preexisting Nb SRF cavity via Sn vapor deposition and infusion.[4,5,13−16] There have been modifications to the Wuppertal growth procedure to preferentially select for growth of the A15 Nb_3Sn phase. Recent work by Posen et al. illustrates a significant difference in Nb_3Sn film quality as a function of Sn flux.[16] In these experiments, Posen et al. increased the flux of $SnCl_2$ during Sn nucleation at 500 °C and Sn vapor during the coating stage at ~1100 °C. This new procedure results in Nb_3Sn that is visually shiny and composed of smaller, smoother grains compared to visually matte coupons with larger, rougher grains. Further studies of the visually shiny
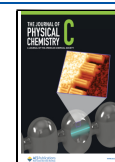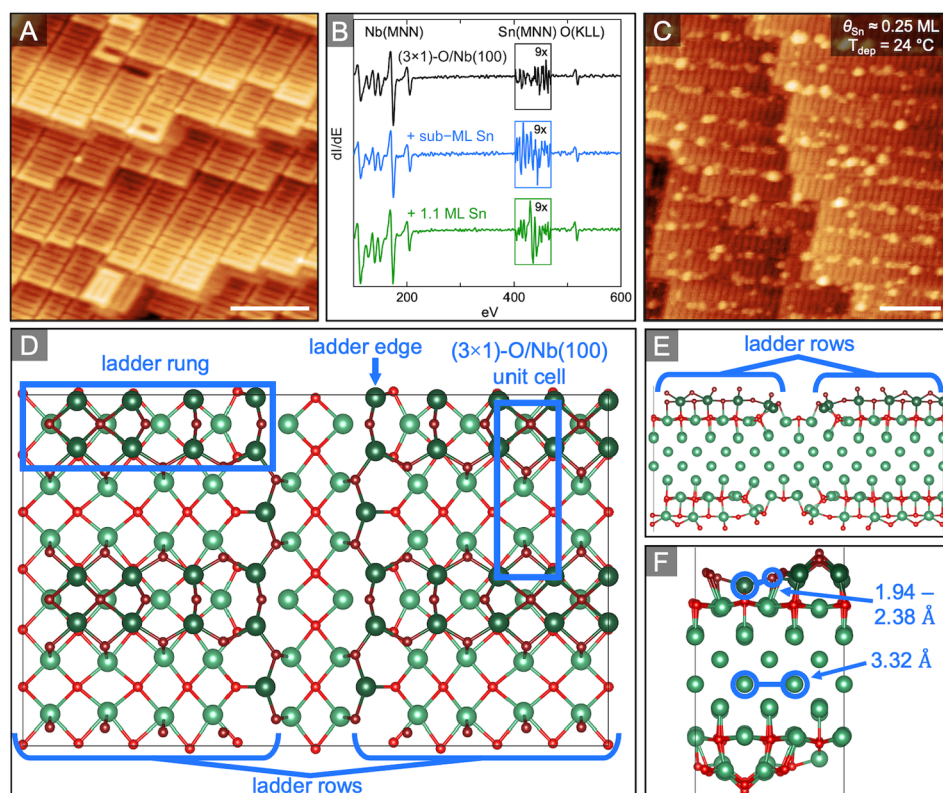
Figure 1. STM, AES, and DFT simulation cell of (3×1)-O/Nb(100) surface before and after Sn exposure. (A) STM image (T_{STM}: 24 °C, scale bar = 10 nm, 40×40 nm²) of the pristine (3×1)-O/Nb(100) surface with highly ordered NbO "ladder" structure extending across terraces. −169 mV, 62 pA. (B) AES spectra of pristine (3×1)-O/Nb(100) surface and (3×1)-O/Nb(100) surface following deposition of sub-ML (0.25 ML) and 1.1 ML Sn. The intensity in the region corresponding to the Sn MNN Auger electron is multiplied by 9 for easier viewing. (C) STM image (T_{STM}: 24 °C, scale bar = 10 nm, 50×50 nm²) of (3×1)-O/Nb(100) following deposition of sub-ML Sn. Bright spots correspond to Sn clusters. 316 mV, 64 pA. (D) Top view of (3×1)-O/Nb(100) DFT simulation cell with the top layer of Nb (green) and O (red) atoms depicted with darker colors. The (3×1)-O unit cell along with ladder edge, row, and rung features are outlined in blue. (E) Side view (3×1)-O/Nb(100) DFT simulation cell consisting of 4 BCC Nb layers with 2 NbO layers on each end containing the (3×1)-O ladder row structure. (F) Second side view of (3×1)-O/Nb(100) DFT simulation cell showing with Nb−Nb inlayer distance and Nb−O distances in the oxide labeled.

Nb₃Sn cavities are needed to understand the relationship between increased Sn flux, grain size and roughness, and cavity performance. Despite these recent advances in Nb₃Sn growth procedures and cavity performance, there is not a thorough overall understanding of which parameters can be tuned during Nb₃Sn growth to preferentially grow the Nb₃Sn A15 phase.

An additional factor when considering Nb₃Sn growth mechanisms on Nb SRF cavity surfaces is the role of the underlying Nb substrate on the surface-mediated growth kinetics and dynamics. Nb readily terminates in an ~5 nm bulk oxide phase, largely composed of pentoxide (Nb_2O_5) with monoxide (NbO) and dioxide (NbO_2) inclusions at the metallic interface.[17] As Nb is heated to temperatures used during Nb₃Sn growth protocols, however, oxygen dissolution into the bulk occurs with primarily the NbO oxide phase remaining on the surface, resulting in a reservoir of interstitial oxygen in the near-surface and bulk of Nb.[17−20] This suggests that under Nb₃Sn growth conditions the oxidized Nb surface is dynamic, and both the NbO surface termination and near-surface oxygen may be significant in Nb₃Sn growth behavior.

Porter et al. found that preanodized Nb SRF cavities with an ~70 nm thick pentoxide capping layer had more uniform Nb₃Sn films with higher performance metrics.[21] While the mechanistic consequences of preanodization on Nb₃Sn growth are not well understood, it is thought that the thicker oxide

layer promotes more uniform Sn nucleation, allowing for homogeneous Nb₃Sn film growth. An oxidized Sn 3d component from X-ray photoelectron spectroscopy (XPS) analysis following Nb₃Sn growth supports Sn−O or Nb−Sn−O coordination occurring within the Nb₃Sn film or at the Nb/Nb₃Sn interfaces.[13,22−24] This highlights the importance of dissolved oxygen species during Nb₃Sn growth procedures. While the Nb oxidation state, composition, and morphology are known to impact the Nb₃Sn film quality, there is interest in determining the role of Nb grain boundaries and near surface defects on Nb₃Sn film quality.[10] It is thought that these material defects may promote Sn diffusion into the Nb bulk, facilitating alloy growth. There are, however, significant stoichiometric variations at grain boundaries. Because of the variation in T_c across the Nb/Sn alloy phase diagram,[11,25] such stoichiometric inhomogeneity can quench superconducting behavior and lower SRF cavity performance. In order to reproducibly fabricate high quality Nb₃Sn SRF cavities, a thorough and mechanistic understanding of the impact of growth conditions, substrate composition and morphology, and Sn−Nb−O interactions on optimal Nb₃Sn film growth is necessary.

The work presented herein visualizes Sn adsorption and diffusion behavior on an oxidized Nb(100) single crystal to investigate the initial Sn/Nb/O interactions guiding Nb₃Sn

growth. Monolayer (ML) and sub-ML quantities of Sn are deposited on a (3×1)-O/Nb(100) surface under ultrahigh-vacuum (UHV) conditions. *In situ* surface analysis via scanning tunneling microscopy (STM) of the sub-ML Sn/(3×1)-O/Nb(100) reveals preferential adsorption of Sn along distinct binding sites on the (3×1)-O unit cell. Annealing the sub-ML and ML Sn/(3×1)-O/Nb(100) samples reveals the formation of hexagonal and rectangular Sn adlayer structures for all Sn coverages studied. Annealing the ML Sn/(3×1)-O/Nb(100) sample drives Sn incorporation into the Nb subsurface, inducing reconstructions to the (3×1)-O/Nb(100) terraces. No such overall reconstruction is found for the sub-ML Sn/(3×1)-O/Nb(100) sample. Additionally, lateral diffusion of the ML Sn/(3×1)-O/Nb(100) sample exhibits distinct evolution of the Sn adlayer with prolonged annealing while no such evolution is observed for the sub-ML sample preparation. These results highlight the significance of growth conditions such as the surface atomic Sn coverage and annealing time in promoting surface-mediated processes that determine the homogeneity and roughness of formed Nb_3Sn films. These experimental results are corroborated by computational results which determine site-specific Sn atom adsorption energies and calculated STM images to confirm structural analysis. This spatially resolved mechanistic information about Sn adsorption and diffusion on an oxidized Nb surface will guide the development of predictive Nb_3Sn growth models needed for the further optimization of Nb_3Sn growth procedures.

■ EXPERIMENTAL AND THEORETICAL METHODS

All experiments were conducted on a Nb(100) single crystal (Surface Preparation Laboratory) in a UHV system equipped with a scanning tunneling microscopy chamber (UHV VT-STM, RHK Technology), preparation chamber, and deposition chamber allowing for *in situ* Sn deposition, sample preparation, and analysis as described elsewhere.[17,18] The (3×1)-O reconstruction (Figure 1A) was formed on the Nb(100) surface via repeated cycles of Ar^+ ion sputtering and annealing at a sample temperature (T_{anneal}) of ~1630 °C as measured using an infrared pyrometer (Mikron Infrared, MG-140). Initial surface cleanliness was confirmed with Auger electron spectroscopy (AES), XPS, and STM analysis. AES analysis measures 11.2 ± 1.3 at. % O in the surface and near-surface region, as shown with a representative spectrum shown in Figure 1B. The clean surface contains a high degree of long-range order, with $4.6 \pm 1.9\%$ of the surface area corresponding to step edges, dislocations, and adatoms.[26] Surface roughness and atomic features on the (3×1)-O surface were calculated using Gwyddion, an open source scanning probe analysis software.

Once surface cleanliness was confirmed, the Nb(100) sample was transferred into the sample stage within the deposition chamber for *in situ* Sn exposure. The Sn was heated via electron beam heating within the crucible of the EFM 3 (Focus GmbH) for several minutes at 1.4 W, as monitored by the EFM 3 control box, to ensure complete melting before opening the shutter for exposure of the Nb(100) sample to Sn. In this work Sn was annealed at 24 W to evaporate with ~150 nA flux as measured by an internal monitor. The (3×1)-O/Nb(100) was exposed to the Sn beam for 30, 60, or 120 s at T_{dep} = 24 °C, resulting in 0.25, 0.5, or 1.1 ML equivalence Sn coverage (θ_{Sn}). The Sn deposition flux was calibrated via quartz crystal microbalance (QCM, INFICON) uptake, and STM analysis of the Nb(100) surface following Sn exposure at

room temperature (Figure 1C) revealed the Sn packing density on the (3×1)-O surface. This allowed for an accurate conversion factor from weight of Sn deposited (in ng) to ML equivalence. For depositions exceeding 1 ML equivalence, the Sn at. % was monitored via AES (Figure 1B). Following Sn deposition, the sample was transferred into the preparation chamber for AES analysis and/or heating to T_{anneal} = 500, 600, 700, 800, or 900 °C before transferring into the STM chamber for spatially resolved analysis of the Sn/Nb(100) sample at an STM temperature (T_{STM}) of 24 °C.

To calculate the site-specific Sn adsorption/binding energy, the density functional theory (DFT) code VASP[27−30] is used with the Perdew−Burke−Ernzerhof approximation[31] for the exchange-correlation functional. The (3×1)-O/Nb(100) structure used in the DFT calculations (Figures 1D−F) consisted of 4 layers of BCC Nb atoms followed by 2 layers of NbO, on both sides of the slab, arranged in the characteristic (3×1) ladder format, as shown in Figure 1D. The final structure is composed of a total of 320 atoms with a vacuum spacing of 10 Å on both sides of the NbO layers. An energy cutoff of 400 eV for the plane-wave basis along with an energy convergence criteria of 10^{-6} eV is used for all the calculations. The structure, without Sn atoms, was first relaxed. The adsorption/binding energy of Sn was evaluated on a total of 14 distinct sites of the slab structure. The middle BCC and bottom ladder layers were fixed while performing structural relaxations with the adsorbed Sn atoms. A k-point density of 6 $\times$ 2 $\times$ 1, which is equivalent to 60 k-points per Å^{-1}, was used in all the DFT calculations. The binding energy is calculated using eq 1

$$ \text{BE} = E_f - E_i - \mu_{Sn} \tag{1} $$

where BE is binding energy and E_f and E_i are the energy of the structure with and without the Sn atom, respectively. For the reference chemical potential of Sn (μ_{Sn}), the energy of the bulk Sn structure is used. Simulated STM images were generated from the DFT data using the ingrained Python package.[32]

■ RESULTS AND DISCUSSION

Sn Adsorption on (3×1)-O/Nb(100). For sub-ML and ML Sn deposition on the (3×1)-O/Nb(100) surface, the AES signal corresponding to the Sn MNN Auger electron is visible in the survey spectra (Figure 1B) taken *in situ* following deposition. Quantitative AES of Sn adsorption on the (3×1)-O was previously reported for exposures between 0.24 and 20 ML which outline the formation of Sn islands as the dominant deposition pathway.[26] STM analysis following deposition of 0.5 and 1.1 ML Sn at T_{dep} = 24 °C showed no clear surface ordering. These higher θ_{Sn} formed a uniform adsorbate layer that was too rough to resolve upon deposition with STM imaging. For θ_{Sn} = 0.25 ML, however, adsorbates laterally diffuse at room temperature to form small 4−6 atom islands arranged along the edges of the ladder row structure (Figure 1C). The sizes of the Sn clusters in Figure 1C were estimated using the lateral and height measurements in the STM image and compared to the atomically resolved STM images of adsorbed Sn presented later. There is no preferential adsorption at other features such as defects or step edges, which are often undercoordinated with lower binding energies,[33,34] and agrees with previous work detailing the role of nanoscale defects on Sn adsorption and diffusion behavior.[26] Metal adatoms on planar metal oxides may diffuse via hopping or long jumps at or below 24 °C.[35−41] While the
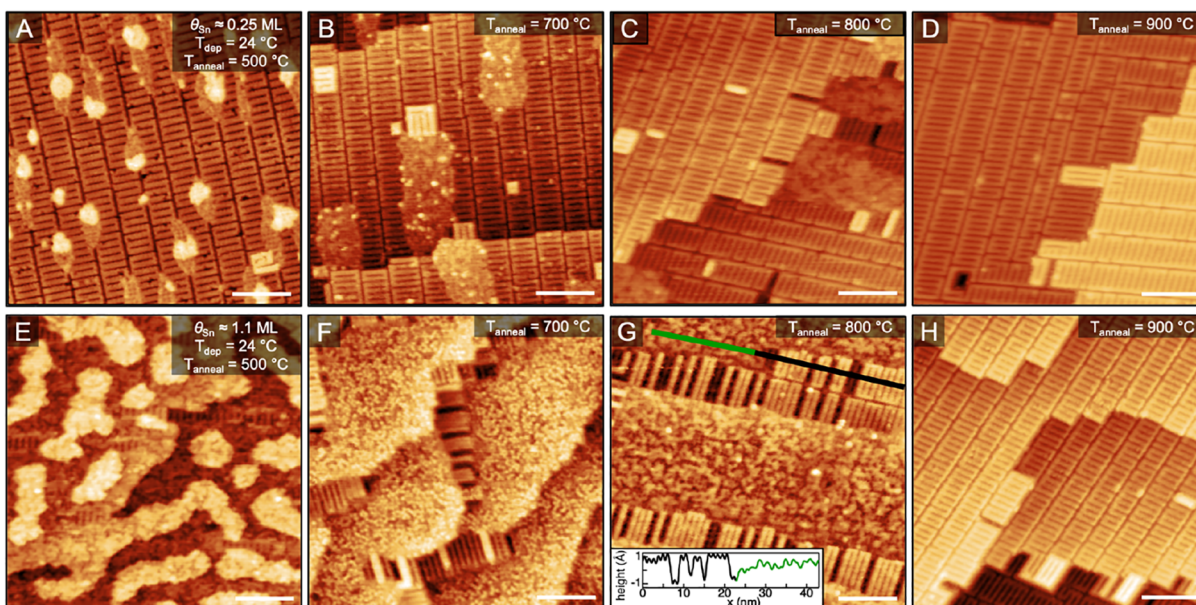
Figure 2. Experimental STM images of Sn adsorption, diffusion, incorporation, and desorption on (3×1)-O/Nb(100). 0.25 ML (A–D) and 1.1 ML (E–H) of Sn were deposited on a (3×1)-O/Nb(100) held at T_{dep}: 24 °C and was subsequently annealed at the indicated T_{anneal} for 5 min preceding STM analysis (T_{STM}: 24 °C, scale bar = 10 nm, 50 × 50 nm^2). Inset line scan in (G) shows Sn adlayer (green) topographically incorporates into the Nb subsurface, disrupting (3×1)-O/Nb(100) terrace (black). STM imaging conditions: (A) 309 mV, 75 pA; (B) −475 mV, −59 pA; (C) −369 mV, −26 pA; (D) 0.64 V, 59.3 pA; (E) 1.38 V, 73 pA; (F) −107 mV, −187 pA; (G) 200 mV, 88 pA; (H) −351 mV, 169 pA.

(3×1)-O oxide is a reconstructed thin oxide with inherent corrugation, the observed aggregation of Sn adatoms uniformly covering the terraces in the sites between (3×1)-O ladder rows, rather than large-scale defects such as step edges, suggests diffusion via hopping or long jumps at room temperature. There is no indication that the Sn adsorbates deviate from essentially, unity sticking, as the deposition rate was calibrated with an inline QCM probe at the same working distance as the sample during deposition. It has also been previously demonstrated that transition metals have near-unity sticking on metal oxide surfaces at room temperature, as the desorption rate is minimal under these conditions.[34,42]

Diffusion Pathways for Submonolayer Sn. Following 0.25 ML Sn deposition at room temperature (Figure 1C), the (3×1)-O/Nb(100) + Sn was sequentially annealed for 5 min at T_{anneal} = 500, 700, 800, and 900 °C (Figures 2A–D, respectively). Following a 5 min anneal at T_{anneal} = 500 °C (Figure 2A), the Sn laterally diffuses to form aggregate islands along the vacancy channels between the (3×1)-O ladder rows. Brighter islands correspond to multilayer aggregates ranging from 5 to 7 ML while the accompanying darker features correspond to monolayer Sn aggregates. STM surveys confirm that Sn islands do not diffuse to preferentially nucleate around large-scale defects such as step edges, similar to the room temperature adsorption behavior observed in Figure 1D. Following the anneal at T_{anneal} = 700 °C in Figure 2B, Sn diffusion is no longer confined between (3×1)-O ladder rows. Rather, the Sn coalesces into larger multilayer islands typically anchored to a step edge and extending across terraces. After annealing to T_{anneal} = 800 °C (Figure 2C), the surface concentration of Sn has decreased, while the underlying (3×1)-O surface structure remains unchanged. Previous work has shown significant degradation of the (3×1)-O ladder structure due to nitrogen substitutional defects and diffusion into the near-surface region of the oxidized Nb(100) crystal.[43]

This lack of perturbation to the (3×1)-O ladder structure suggests that Sn desorption, rather than incorporation into the near-surface region, is the dominant process. Further evidence comes from an anneal at T_{anneal} = 900 °C, where the Sn has fully desorbed from the surface. For the thermally driven diffusion of 0.25 ML Sn, Sn adsorption and diffusion are primarily guided by the underlying structure of the (3×1)-O surface; the oxide structure of the Nb surface influences the relative diffusion and desorption behavior. Specifically, the vacancy channels between the (3×1)-O rows enable the lateral diffusion of Sn into ordered Sn adlayers but do not enable incorporation and alloying. For submonolayer coverages of Sn on the (3×1)-O/Nb(100) surface, Sn desorption occurs before the critical alloy formation threshold between approximately 850 and 920 °C.[25,44]

Diffusion Pathways for Monolayer Sn. The relationship between Sn coverage and Sn adsorption and diffusion behavior for θ_{Sn} = 1.1 ML deposited at room temperature and subsequently annealed at T_{anneal} = 500, 700, 800, and 900 °C is shown in Figures 2E–H, respectively. The Sn laterally diffuses following a 5 min anneal at T_{anneal} = 500 °C (Figure 2E), forming Sn islands which extend across the (3×1)-O surface, leaving only a small proportion of the underlying (3×1)-O surface exposed. STM survey scans confirm uniform Sn coverage, with no preferential adsorption to larger scale defects. As observed for the submonolayer case, the brighter islands in Figure 2E have a height of 5−7 ML, while the darker islands are monolayer regions. When annealed at T_{anneal} = 700 °C (Figure 2F), the diffusion pathways for Sn for the 1.1 ML exposure deviate from those observed for submonolayer Sn exposure; the Sn fully engulfs the sharp (3×1) step edges, and reconstructions across the NbO terraces are observed. As with the lower θ_{Sn}, there does not appear to be significant Sn desorption following the 700 °C anneal. It is evident the balance between Sn desorption, lateral diffusion, and

incorporation is not only highly sensitive to temperature, but the total coverage of Sn aids in promoting incorporation at lower temperature thresholds. This is further illustrated upon annealing at T_{anneal} = 800 °C, as Figure 2G shows complete Sn incorporation into the (3×1)-O ladders as indicated by the relative topographical height of the Sn adlayers. Furthermore, reconstructions of the (3×1) unit cell upon Sn diffusion and incorporation are not observed for submonolayer Sn coverages and indicate a new diffusion and incorporation mechanism for higher Sn coverages. Sn incorporation is an essential process for Nb_3Sn growth via Sn vapor deposition procedures. It is thought that Nb_3Sn growth is facilitated by Sn diffusion into the Nb bulk at grain boundaries. This incorporation behavior suppresses Sn desorption and increases the Sn concentration gradient throughout the near-surface region during Nb_3Sn growth procedures. Maintaining higher surface and near-surface concentrations of Sn through incorporation mechanisms prevents the formation of Sn-deficient regions, which are commonly observed in actual Nb_3Sn cavity coupons.[45] Annealing at T_{anneal} = 900 °C (Figure 2H), within the range of reported temperature thresholds for Nb_3Sn alloy formation,[25,44] it is evident that all Sn has desorbed from the surface. AES and XPS analyses of the crystal following the 900 °C anneal confirm the lack of near-surface Sn. Figure 2H depicts jagged (3×1) projections at the step edges that are not present on pristine (3×1)-O/Nb(100) or following submonolayer Sn adsorption and diffusion experiments. These step edge protrusions are direct evidence of the surface reconstructions that occur due to Sn incorporating through the (3×1)-O surface following annealing at $T_{anneal} \cong$ 700−800 °C. Sn incorporation through the Nb oxide surface layer is the initial step for the formation of a Nb_3Sn intermetallic layer. Moreover, the growth of a homogeneous Nb_3Sn film relies upon Sn incorporation via bulk diffusion through the forming intermetallic layer to access elemental bulk Nb for continued growth. The observed incorporation of 1.1 ML of Sn into the subsurface following annealing at T_{anneal} = 800 °C is a direct consequence of the increased Sn concentration at the Sn/(3×1)-O/Nb(100) interface. As previously noted, the ordered (3×1)-O surface persists at high temperatures exceeding 850 °C.[19] Therefore, the incorporation of Sn and resulting disruption of the (3×1)-O periodic structure were induced by this increased Sn concentration.

The observed Sn desorption at T_{anneal} = 900 °C suggests that alloy formation is highly unlikely for the Sn coverages probed in this study. Recent work indicates that Sn alloyed with Nb persists on the surface between 950 and 1100 °C, beyond which Sn desorption occurs, while nonalloyed Sn desorbs at significantly lower temperatures.[46] To promote the formation of desired Nb/Sn alloys, it is important to facilitate Sn subsurface incorporation during deposition procedures and prevent Sn loss to desorption upon thermal annealing. Our results show that for lower Sn coverages, desorption is a competing process at the temperatures (Figure 2C) used to induce incorporation and eventual formation of the alloy interface, especially for lower Sn concentrations at the NbO surface. While industrial scale Nb_3Sn growth involves depositing Sn at higher fluxes, the propensity for Sn island aggregation on Nb surfaces likely prevents the formation of a uniform Sn wetting layer, producing extensive Sn-deficient regions throughout the alloy film. Ongoing studies are currently underway to further examine how substrate temperature during both deposition and postdeposition annealing

impacts the extent of Sn surface incorporation, thermal stability of formed adlayers, and formation of intermetallic species.

Coverage-Dependent Kinetic Barriers to Sn Lateral Diffusion. Prolonged Sn nucleation, coating, and postcoating annealing procedures are used for actual Nb_3Sn SRF cavity production to form smoother, more homogeneous Nb_3Sn films.[16] To determine the kinetic behavior influencing Sn diffusion and promoting Sn adlayer smoothening on the (3×1)-O surface, Figures 3A−D show submonolayer and
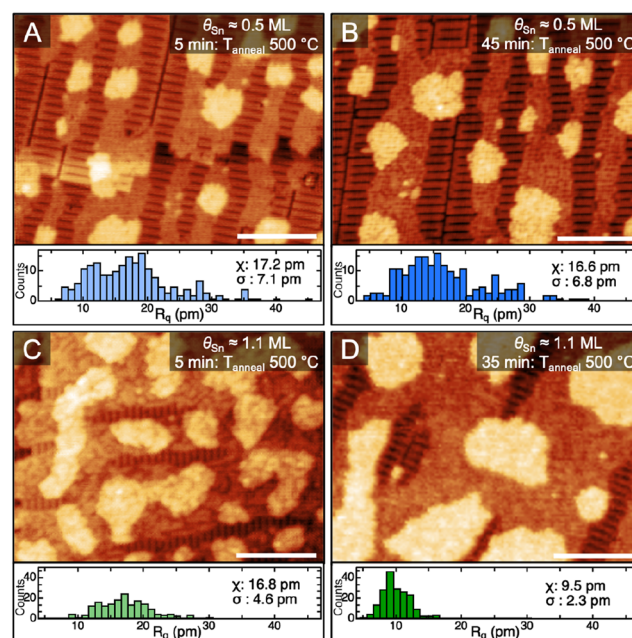

Figure 3. Experimental STM images detailing coverage-dependent kinetics of Sn lateral diffusion (T_{STM}: 24 °C, scale bar = 10 nm, 40 × 30 nm^2). 0.5 ML (A, B) and 1.1 ML (C, D) of Sn on (3×1)-O/Nb(100) were annealed for varying durations at T_{anneal}: 500 °C before imaging. Each inset histogram depicts surface roughness (R_q) values for 200 sampled Sn adlayers along with the R_q distribution averages (χ) and standard deviations (σ). Histograms contain R_q values obtained from multiple images obtained with varying STM imaging conditions. (A) 0.5 ML of Sn, 5 min at T_{anneal}: 500 °C. −237 mV, −118 pA; (B) 0.5 ML of Sn, 45 min at T_{anneal}: 500 °C. 295 mV, −122 pA; (C) 1.1 ML of Sn, 5 min at T_{anneal}: 500 °C. 0.75 V, 139 pA; (D) 1.1 ML of Sn, 35 min at T_{anneal}: 500 °C. 44.5 mV, 129 pA.

monolayer equivalent doses of Sn deposited on (3×1)-O/Nb(100) were annealed for varying lengths of time at T_{anneal} = 500 °C. As was the case in Figure 2, the darker Sn islands in Figure 3 are approximately 1 ML thick and the brighter islands are up to 7 ML thick. In Figure 3C, the higher coverage of Sn deposited results in a higher concentration of bright islands compared to the darker ML adlayers. The inset histograms display the surface roughness (R_q) of the resultant Sn adlayers. A slightly higher submonolayer coverage (0.5 ML) of Sn was deposited at T_{dep} = 24 °C on (3×1)-O/Nb(100) and annealed at 500 °C for 5 min (Figure 3A) and 45 min (Figure 3B) with *in situ* STM analysis following the thermal treatments. Continued annealing at T_{anneal} = 500 °C does not drastically change the roughness of the 0.5 ML Sn adlayer on the surface, as there is only a slight reduction in the R_q distribution average and standard deviation for the longer anneal. After a 5 min anneal at T_{anneal} = 500 °C of the sample with θ_{Sn} = 1.1 ML
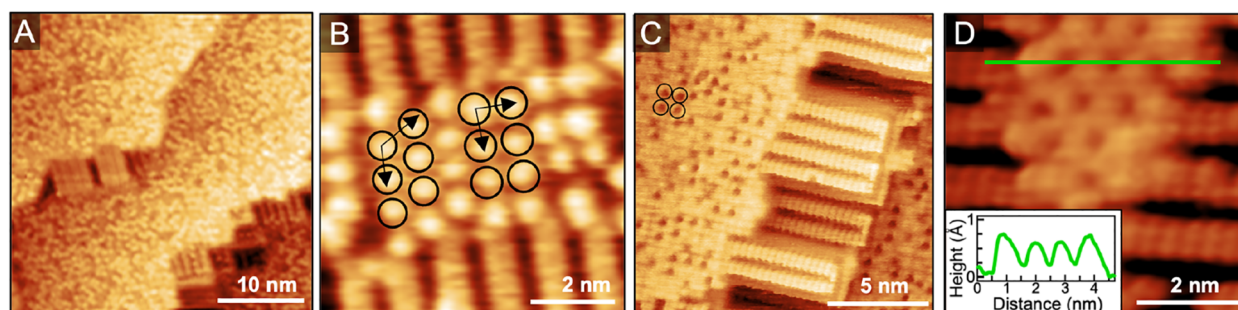
Figure 4. Experimental STM images depicting atomic arrangement of Sn adlayers resulting from varying deposition lengths and annealing conditions (T_{STM}: 24 °C, scale bar and image size vary). (A) 1.1 ML Sn + 700 °C. −0.107 V, 187 pA; (B) 0.5 ML + 700 °C. Hexagonal and rectangular Sn atomic packing arrangements outlined in black with arrows corresponding to lattice parameters of 8.4 and 8.0 nm, respectively. 0.80 V, 77 pA; (C) 1.1 ML Sn + 800 °C. Voided Sn adlayer regions outlined by black circles. −0.078 V, 125 pA; (D) 0.25 ML + 600 °C. Hexagonally arranged Sn atomic positions corresponding to topographical depressions, shown in inset line scan, −0.192 V, 84.9 pA.
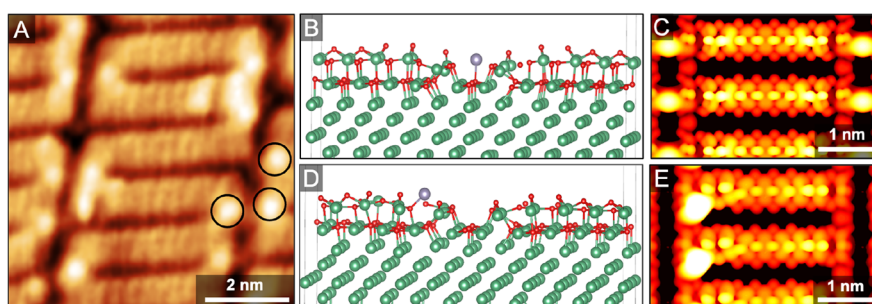
Figure 5. Experimental and simulated STM images along with simulation cells of individual Sn atoms adsorbed on (3×1)-O/Nb(100) (T_{STM}: 24 °C; scale bar and image size vary). Simulated STM do not have any discernible dependence on bias voltage or tunneling current. (A) 0.5 ML + 700 °C. Black circles denote individual Sn atoms. −0.82 V, 69 pA. (B, C) Simulation cell and STM of Sn adsorption site between the (3×1)-O/Nb(100) ladder edges. −1.59 eV/atom. (D, E) Simulation cell and STM of Sn adsorption site near the (3×1)-O/Nb(100) ladder edges −1.51 eV/atom.

(Figure 3C), there is minimal evolution in the roughness of the Sn adlayers, similar to the 0.5 ML Sn adlayers in Figures 3A,B. However, annealing the $\theta_{Sn} = 1.1$ ML Sn sample for 35 min results in a smoother and more uniform Sn adlayer in Figure 3D. Regardless of the θ_{Sn} present on the (3×1)-O surface and the annealing time at $T_{anneal} = 500$ °C, there is no decrease in Sn coverage and the overall Sn adlayer structures are not fundamentally changed. This illustrates that at lower Sn coverages, the length of time spent at the nucleation temperature of 500 °C does not significantly change the Sn adsorbate structures. Additionally, lateral diffusion along the (3×1)-O ladder row structure is the dominant diffusion pathway at temperatures used during the nucleation steps for industrial-scale growth.

Fine Structure of Sn Adlayers. While Sn coverage, annealing temperatures, and annealing times strongly influence Sn adsorption and diffusion behavior, the Sn adlayers studied in this work display consistency in the atomic configurations within the imaged Sn adlayers, as shown in Figure 4. The Sn adlayers experimentally observed on (3×1)-O/Nb(100) adopted either a rectangular-packed or hexagonal-packed atomic arrangement.

Figures 4A and 4B show the Sn atoms imaged as spherical protrusions for monolayer and submonolayer coverages, respectively. In Figure 4A, a 1.1 ML equivalence of Sn deposited at $T_{dep} = 24$ °C was annealed at $T_{anneal} = 700$ °C, resulting in near-complete wetting of the surface. Sn adlayers completely cover the terrace, covering the square (3×1)-O/Nb(100) step edges, with some step edge reconstruction seen

as NbO rectangular protrusions from rounded Sn covered step edges, as was shown in Figure 2F. For the submonolayer Sn/(3 × 1)-O/Nb(100) sample preparation shown in Figure 4B, the surface was exposed to 0.5 ML equivalence Sn and annealed at $T_{anneal} = 500$ °C. This resulted in similar Sn adlayer features along the edges of the (3×1)-O/Nb(100) structure as described in Figure 2A. While the total Sn surface coverage varies between Figure 4A and Figure 4B, the bright protrusions in both images form consistent hexagonal and rectangular packed Sn structures. The protrusions outlined in black in Figure 4B highlight the two distinct packing arrangements: a hexagonal packing with an 8.4 Å lattice parameter and a rectangular packing arrangement with a lattice parameter of 8 Å. Both a hexagonal and a rectangular packing structure have been observed for Sn adlayers on metallic Nb(110) but have not been previously reported on oxidized Nb.[47]

The rectangular packing structure appears to be guided by the underlying (3×1)-O structure due to the arrangement of the bright protrusions relative to the (3×1)-O unit cell. The hexagonal and rectangular Sn structures coexist in the same Sn adlayer islands with no apparent preferred structure across the submonolayer samples. The hexagonal packing structure is, however, more commonly observed for the monolayer Sn coverages, such as that shown in Figure 4A, due to the increased thickness of the Sn adlayers; this prevents the underlying (3×1)-O surface from effectively templating the Sn adlayer into the rectangular packing structure.

It is interesting to note that depending on the imaging bias and STM tip morphology, the hexagonal and rectangular

structures can be imaged as protrusions (Figures 4A,B) or depressions (Figures 4C,D) across experimental trials. Figure 4C shows θ_{Sn} = 1.1 ML annealed at T_{anneal} = 800 °C inducing Sn incorporation into Nb, resulting in reconstruction of the (3 × 1)-O/Nb(100) surface, previously shown in Figure 2G. Surrounding the disrupted NbO structure is the partially wetted Sn layer with voided regions that contain some rectangular long-range order denoted by black outlined circles. The structural configuration of the Sn adlayers is not clear in this case, but for 0.5 ML equivalence Sn annealed to 500 °C in Figure 4D, it becomes more apparent that these depressions correspond to positions of Sn atoms. The hexagonal spacing in this case closely corresponds with that observed for the protruding Sn atoms in Figures 4A and 4B. Now, rather than the Sn imaging as bright protrusions, the negative bias induces tunneling from the empty states above the Fermi level, resulting in Sn appearing as depressions.

Experimental and DFT Simulated Data of Individual Adsorbed Sn Atoms. Annealing the submonolayer Sn/(3 × 1)-O sample predominantly forms Sn islands along the ladder rows; however, individual Sn atoms were also imaged on the (3 × 1)-O/Nb(100) ladder edge sites (Figure 5A). Sn atoms largely adsorbed to the edges of the (3 × 1)-O/Nb(100) ladder rungs corresponding to the Nb atom bridging each rung. Contrasting to the hexagonal and rectangular packed adlayers shown in Figure 4, there was no observed tip or bias dependence on the topography or electronic distribution of these individual Sn atoms.

To determine the most favorable binding sites for a single adsorbed Sn atom, DFT calculations were employed. The (3 × 1)-O/Nb(100) simulation cell without Sn atoms was first relaxed. The Nb−Nb in-layer distance in the BCC layers of the structure is 3.32 Å. The Nb−O distance in the oxide layer varies between ∼1.94 and 2.38 Å as shown in Figure 1F. For comparison, the Nb−O distance in bulk NbO is about 2.10 Å.[48] In total, binding energies of 14 sites were calculated. Among these sites, simulated STM images were generated for the two with the lowest adsorption energy sites in Figures 5B and 5D. These lowest binding energy sites correspond to the top of the ladder rungs between (Figure 5B) and near (Figure 5D) the (3 × 1)-O/Nb(100) ladder edges. Figures 5C and 5E show the simulated STM images of the (3 × 1)-O/Nb(100) ladder structure with adsorbed Sn. These two sites have binding site energies of −1.59 and −1.51 eV per adsorbed Sn atom, respectively, indicative of favorable Sn atom adsorption sites. In Figures 5C and 5E, the brightness of the simulated STM image indicates regions of high electron density. The Sn atom in Figure 5C is located between two ladder edges, topographically below the surrounding (3 × 1)-O/Nb(100) surface structure, reducing the observed brightness for Sn atoms at this adsorption site. As a result of this, the brightness of the Sn atom in the simulated STM image is comparable to other atoms on the surface. Thus, experimental STM data may not clearly distinguish Sn atoms adsorbed at this site. On the other hand, the topographical distinction of individual Sn atoms adsorbed near the ladder edges (Figure 5D) provides much more contrast for the simulated STM tip, resulting in a much brighter appearance than the surrounding ladder structure (Figure 5E). While the Sn adsorbed between the ladder row structure may be present in the experimental STM data, the simulated STM image of Sn adsorbed at the ladder edge sites in Figure 5D corresponds closely to the morphology of individual Sn atoms from experimental STM data. The

appearance of Sn as bright protrusions in Figure 5A is reflective of the indicated binding site topography as well as the high density of states across the probed simulated and experimental imaging conditions.

DFT and Experimental Data of Sn Adlayer Stability on NbO. On the basis of the measured distance between adjacent Sn atoms, it appears that the hexagonal and rectangular islands of the adsorbed Sn are incommensurate with the underlying substrate. We base this conclusion on the lattice parameter of the substrate. In the DFT relaxed (3 × 1)-O/Nb(100) ladder structure, the distance between adjacent oxygen atoms (and adjacent Nb atoms) varies depending on whether the oxygen atoms are near the edge of the ladder or in between the ladder rungs. Because of these varying adjacent oxygen atom distances, a planar FCC NbO(100) surface[49] is used as a reference for lattice parameters. For a planar NbO(100) surface without the reconstructions forming the (3 × 1) unit cell, the oxygen atoms form an FCC lattice with a lattice parameter of 4.51 Å, and the distance between the nearest oxygen neighbors is 3.19 Å. Comparing these distances with the apparent lattice parameters of the hexagonal (8.4 Å) and rectangular (8.62 × 8 Å) arrangement of Sn atoms, it is clear that the Sn atomic arrangement is incommensurate with the underlying NbO substrate. The incommensurate nature of the Sn adlayers is experimentally supported by the adlayers being predominantly anchored over the regions between the (3 × 1) row structure (shown clearly in the submonolayer cases in Figures 2A,B), with desorption processes occurring at temperatures necessary to induce complete wetting of the surface (Figures 2C,D). While this centering over the ladder edge regions is more difficult to discern for the monolayer Sn coverage (Figures 2E,F), the Sn does not fully wet the (3 × 1)-O/Nb(100) surface, and any incorporation at 800 °C (Figure 2G) is ultimately dominated by full desorption at 900 °C (Figure 2H). Therefore, this observed hexagonal and rectangular ordering of Sn islands does not indicate a preferred wetting layer. The calculations reinforce the experimental finding that there is no propensity to form a commensurate Sn layer on the (3 × 1)-O/Nb(100) surface. The thermal persistence of the Sn adlayers up to 800 °C does, however, suggest some degree of additional adlayer stabilization, perhaps from many-body effects involving the oxide substrate and adsorbed Sn atoms.

■ CONCLUSION

In this work, we demonstrate submonolayer and monolayer Sn adsorption and diffusion behavior on an oxidized Nb(100) surface. By utilizing (3 × 1)-O/Nb(100), a highly ordered and well-characterized NbO reconstruction, in a UHV chamber with *in situ* surface preparation and analysis capabilities, thermally activated Sn surface behavior at temperatures relevant to Nb$_3$Sn growth has been visualized with atomic precision. At submonolayer coverages, Sn diffuses to form uniform islands between the ladder structures on (3 × 1)-O/Nb(100) at room temperature. Sn did not aggregate at large-scale surface defects; rather, atomic sites in the (3 × 1)-O unit cell guide Sn diffusion. The (3 × 1)-O structure continues to dictate Sn behavior upon annealing between 500 and 900 °C, as Sn laterally diffuses to form larger islands within the constraints imposed by the (3 × 1)-O ladder structures before either desorption or incorporation into the (3 × 1)-O surface occurs.

There is also an observed coverage dependence to the Sn diffusion kinetics; continued annealing of monolayer Sn coverages at 500 °C showed a significant reduction in the average roughness and distribution of Sn islands. This suggests that the heating ramp rates and total time at specific temperatures in Sn coating furnaces may affect Sn behavior differently depending on the vapor flux and Sn source geometry while coating Nb SRF cavities. At 700 °C there is a stark difference in monolayer Sn behavior, as adsorbates perturb the underlying Nb(100) surface, indicated by disruptions in the (3×1)-O/Nb(100) unit cell and rounding of the BCC step edges. Approaching the Nb$_3$Sn alloy formation temperature, the Sn incorporates into the substrate at 800 °C, an early incorporation step that was not observed in the submonolayer case. While the Sn desorbed from the surface by 900 °C, the (3×1)-O/Nb(100) was recovered with observed damage signaling regions of Sn incorporation. While the change in Sn concentration seems subtle, the increase from 0.25 to 1.1 ML was enough to dramatically alter Sn behavior. This increase promoted Sn incorporation and suppressed desorption rates at 800 °C, demonstrating atomic-scale differences such as the local Sn concentration at the interface dramatically impacts the formation of Sn-deficient sites at temperatures probed in the alloy growth procedure.

We also report the fine structure of the observed Sn adlayers, with two distinct morphologies: (1) hexagonal packing and (2) rectangular packing, along with individual Sn atoms adsorbed on (3×1)-O/Nb(100) ladder edge sites. Both experimental STM images and simulated data conclude that these hexagonal and rectangular Sn islands are incommensurate with the (3×1)-O/Nb(100) surface. The DFT-derived STM images and binding energies for individual Sn adsorption sites are in close agreement with our experimental observations.

In these studies, we explore the adsorption and nucleation dynamics of Sn monolayer and multilayer structures on a highly ordered Nb oxide surface. We show that the atomic sites on the (3×1)-O/Nb(100) surface play a leading role in driving the relative rates of Sn adsorption and surface binding, desorption, bulk incorporation, and intermetallic growth. The lack of a complete Sn wetting layer, desorption below the Nb$_3$Sn formation temperature, and limited stable surface binding sites are all indicative of a Sn/Nb interface ill-suited for homogeneous Nb$_3$Sn growth. Additionally, substantial efforts are being made to consider the role of the chemical composition of Nb surfaces in optimizing Nb$_3$Sn films, but we still lack a comprehensive understanding of how the diversity of Nb oxide compositions, thicknesses, and structures impact alloy quality. While the chemical surface composition certainly impacts Sn—substrate interactions, we have demonstrated that the Nb nanoscale surface morphology also serves as a mechanistic bottleneck in trying to promote homogeneous Nb—Sn alloy growth.

Understanding the initial surface-mediated behavior of Sn adsorbates on oxidized Nb is critical for developing a predictive model of idealized Nb$_3$Sn alloy growth from Sn vapor deposition. Altering the Nb—Sn interface through methods such as including a chlorinated Sn nucleating agent or modifying the Nb surface oxide supports the concept that Sn surface diffusion behavior significantly affects alloy diffusion pathways. Without an understanding of Sn adsorption energies and diffusion pathways on Nb oxides at varying concentrations and thermal treatments, a more predictive model for Nb$_3$Sn growth cannot be developed. The reported findings begin to

answer some of these critical questions, as part of the collective effort to optimize industrial-scale Nb$_3$Sn growth and SRF performance.

■ AUTHOR INFORMATION

Corresponding Author

S. J. Sibener − *The James Franck Institute and Department of Chemistry, The University of Chicago, Chicago, Illinois 60637, United States;* ⬤ orcid.org/0000-0002-5298-5484; Email: s-sibener@uchicago.edu

Authors

Sarah A. Willson − *The James Franck Institute and Department of Chemistry, The University of Chicago, Chicago, Illinois 60637, United States*

Rachael G. Farber − *The James Franck Institute and Department of Chemistry, The University of Chicago, Chicago, Illinois 60637, United States;* Present Address: Department of Chemistry, The University of Kansas, 1567 Irving Hill Rd, Lawrence, Kansas 66045

Ajinkya C. Hire − *Department of Materials Science and Engineering Herbert Wertheim College of Engineering, University of Florida, Gainesville, Florida 32611, United States; Quantum Theory Project, University of Florida, Gainesville, Florida 32611, United States*

R. G. Hennig − *Department of Materials Science and Engineering Herbert Wertheim College of Engineering, University of Florida, Gainesville, Florida 32611, United States; Quantum Theory Project, University of Florida, Gainesville, Florida 32611, United States;* ⬤ orcid.org/ 0000-0003-4933-7686

Complete contact information is available at: https://pubs.acs.org/10.1021/acs.jpcc.2c08458

Author Contributions

S.A.W. and R.G.F. are co-first authors.

Notes

The authors declare no competing financial interest.

■ REFERENCES

(1) Padamsee, H.; Knobloch, J.; Hays, T. *RF Superconductivity for Accelerators*, 2nd ed.; Wiley-VCH: 2008.

(2) Padamsee, H. *RF Superconductivity: Science, Technology, and Applications*, 1st ed.; Wiley-VCH: 2009.

(3) Antoine, C. Materials, and Surface Aspects in the Development of SRF Niobium Cavities; EuCARD-BOO-2012-001; EuCARD Editorial Series on Accelerator Science, Warsaw, Poland, 2012.

(4) Posen, S.; Liepe, M. Advances in Development of Nb$_3$Sn Superconducting Radio-Frequency Cavities. *Phys. Rev. Spec. Top. - Accel. Beams* **2014**, *17* (11), 112001.

(5) Posen, S.; Hall, D. L. Nb3Sn Superconducting Radiofrequency Cavities: Fabrication, Results, Properties, and Prospects. *Supercond. Sci. Technol.* **2017**, *30* (3), No. 033004.

(6) Stilin, N.; Holic, A.; Liepe, M.; Porter, R.; Sears, J. Stable CW Operation of Nb$_3$Sn SRF Cavity at 10 MV/m Using Conduction Cooling. arXiv: 2002.11755 [physics.acc-ph], 2020.

(7) Posen, S.; Liepe, M.; Hall, D. L. Proof-of-Principle Demonstration of Nb$_3$Sn Superconducting Radiofrequency Cavities for High Q$_0$ Applications. *Appl. Phys. Lett.* **2015**, *106* (8), No. 082601.

(8) Dhuley, R. C.; Posen, S.; Geelhoed, M. I.; Prokofiev, O.; Thangaraj, J. C. T. First Demonstration of a Cryocooler Conduction Cooled Superconducting Radiofrequency Cavity Operating at Practical Cw Accelerating Gradients. *Supercond. Sci. Technol.* **2020**, *33* (6), 06LT01.

(9) Transtrum, M. K.; Catelani, G.; Sethna, J. P. Superheating Field of Superconductors within Ginzburg-Landau Theory. *Phys. Rev. B* **2011**, *83* (9), No. 094505.

(10) Kelley, M. M.; Sitaraman, N. S.; Arias, T. A. Ab Initio Theory of the Impact of Grain Boundaries and Substitutional Defects on Superconducting Nb$_3$Sn. *Supercond. Sci. Technol.* **2021**, *34* (1), No. 015015.

(11) Godeke, A. A Review of the Properties of Nb$_3$Sn and Their Variation with A15 Composition, Morphology and Strain State. *Supercond. Sci. Technol.* **2006**, *19* (8), R68−R80.

(12) Porter, R. D.; Hall, D. L.; Liepe, M.; Maniscalco, J. T. Surface Roughness Effect on the Performance of Nb$_3$Sn Cavities. *Proceedings of LINAC2016*, East Lansing, MI, September 25−30, 2016; JACoW; 2017; Vol. *4*, pp 129−132.

(13) Heinrichs, H.; Arnolds-Mayer, G.; Grundey, T.; Klein, U.; Minatti, N.; Mueller, G.; Peiniger, M.; Piel, H.; Unterboersch, G.; Vogel, H. P. Activities on RF-Superconductivity at Wuppertal; Proceedings of the Second Workshop on RF Superconductivity, Geneva, Switzerland, July 23−27, 1984; pp 141−170.

(14) Peiniger, M. Herstellung Und Test Eines S-Band Resonators Mit Nb$_3$Sn Oberflache. Ph.D. Thesis, University of Wuppertal: Wuppertal, Germany, 1983.

(15) Peiniger, M.; Hein, M.; Klein, N.; Mueller, G.; Piel, H.; Thuenus, P. Work on Nb$_3$Sn Cavities at Wuppertal; Proceedings of The Third Workshop on RF Superconductivity, Argonne National Laboratory, Lemont, IL, September 14−18, 1987; Argonne National Laboratory: Lemont, IL, 1988; pp 503−531.

(16) Posen, S.; Lee, J.; Seidman, D. N.; Romanenko, A.; Tennis, B.; Melnychuk, O. S.; Sergatskov, D. A. Advances in Nb$_3$Sn Superconducting Radiofrequency Cavities towards First Practical Accelerator Applications. *Supercond. Sci. Technol.* **2021**, *34* (2), No. 025007.

(17) Oechsner, H.; Giber, J.; Füßer, H. J.; Darlinski, A. Phase Transition and Oxide Dissolution Processes in Vacuum-Annealed Anodic Nb$_2$O$_5$/Nb Systems. *Thin Solid Films* **1985**, *124* (3), 199−210.

(18) Veit, R. D.; Kautz, N. A.; Farber, R. G.; Sibener, S. J. Oxygen Dissolution and Surface Oxide Reconstructions on Nb(100). *Surf. Sci.* **2019**, *688*, 63−68.

(19) McMillan, A. A.; Graham, J. D.; Willson, S. A.; Farber, R. G.; Thompson, C. J.; Sibener, S. J. Persistence of the Nb(100) Surface Oxide Reconstruction at Elevated Temperatures. *Supercond. Sci. Technol.* **2020**, *33* (10), 105012.

(20) Grundner, M.; Halbritter, J. On Surface Coatings and Secondary Yield of Nb$_3$Sn and Nb. *J. Appl. Phys.* **1980**, *51* (10), 5396−5405.

(21) Porter, R.; Arias, T.; Cueva, P.; Hall, D.; Liepe, M.; Maniscalco, J.; Muller, D.; Sitaraman, N. Next Generation Nb$_3$Sn SRF Cavities for Linear Accelerators. Proceedings of LINAC2018, Beijing, China, September 16−21, 2018; JACoW; 2019; pp 462−465.

(22) Miller, J. N.; Lindau, I.; Stefan, P. M.; Weissman, D. L.; Shek, M. L.; Spicer, W. E. Photoemission Studies of Clean and Oxidized Nb and Nb$_3$Sn. *J. Appl. Phys.* **1982**, *53* (4), 3267−3271.

(23) Darlinski, A.; Halbritter, J. Angle-Resolved XPS Studies of Oxides at NbN, NbC, and Nb Surfaces. *Surf. Interface Anal.* **1987**, *10* (5), 223−237.

(24) Pudasaini, U.; Eremeev, G. V.; Reece, C. E.; Tuggle, J.; Kelley, M. J. Initial Growth of Tin on Niobium for Vapor Diffusion Coating of Nb$_3$Sn. *Supercond. Sci. Technol.* **2019**, *32* (4), No. 045008.

(25) Charlesworth, J. P.; Macphail, I.; Madsen, P. E. Experimental Work on the Niobium-Tin Constitution Diagram and Related Studies. *J. Mater. Sci.* **1970**, *5* (7), 580−603.

(26) Farber, R. G.; Willson, S. A.; Sibener, S. J. Role of Nanoscale Surface Defects on Sn Adsorption and Diffusion Behavior on Oxidized Nb(100). *J. Vac. Sci. Technol. A* **2021**, *39* (6), No. 063212.

(27) Kresse, G.; Hafner, J. Ab Initio Molecular Dynamics for Liquid Metals. *Phys. Rev. B* **1993**, *47* (1), 558−561.

(28) Kresse, G.; Hafner, J. Ab Initio Molecular-Dynamics Simulation of the Liquid-Metal−Amorphous-Semiconductor Transition in Germanium. *Phys. Rev. B* **1994**, *49* (20), 14251−14269.

(29) Kresse, G.; Furthmüller, J. Efficiency of Ab-Initio Total Energy Calculations for Metals and Semiconductors Using a Plane-Wave Basis Set. *Comput. Mater. Sci.* **1996**, *6* (1), 15−50.

(30) Kresse, G.; Furthmüller, J. Efficient Iterative Schemes for Ab Initio Total-Energy Calculations Using a Plane-Wave Basis Set. *Phys. Rev. B* **1996**, *54* (16), 11169−11186.

(31) Perdew, J. P.; Burke, K.; Ernzerhof, M. Generalized Gradient Approximation Made Simple. *Phys. Rev. Lett.* **1996**, *77* (18), 3865−3868.

(32) Schwenker, E.; Kolluru, V. S. C.; Guo, J.; Zhang, R.; Hu, X.; Li, Q.; Paul, J. T.; Hersam, M. C.; Dravid, V. P.; Klie, R.; Guest, J. R.; Chan, M. K. Y. Ingrained: An Automated Framework for Fusing Atomic-Scale Image Simulations into Experiments. *Small* **2022**, *18* (19), 2102960.

(33) Diebold, U.; Lehman, J.; Mahmoud, T.; Kuhn, M.; Leonardelli, G.; Hebenstreit, W.; Schmid, M.; Varga, P. Intrinsic Defects on a TiO$_2$(110)(1 × 1) Surface and Their Reaction with Oxygen: A Scanning Tunneling Microscopy Study. *Surf. Sci.* **1998**, *411* (1), 137−153.

(34) Bäumer, M.; Freund, H.-J. Metal Deposits on Well-Ordered Oxide Films. *Prog. Surf. Sci.* **1999**, *61* (7), 127−198.

(35) Ferrando, R.; Fortunelli, A. Diffusion of Adatoms and Small Clusters on Magnesium Oxide Surfaces. *J. Phys.: Condens. Matter* **2009**, *21* (26), 264001.

(36) Barcaro, G.; Fortunelli, A. Structure and Diffusion of Small Ag and Au Clusters on the Regular MgO (100) Surface. *New J. Phys.* **2007**, *9* (2), 22−22.

(37) Barcaro, G.; Fortunelli, A.; Nita, F.; Ferrando, R. Diffusion of Palladium Clusters on Magnesium Oxide. *Phys. Rev. Lett.* **2005**, *95* (24), 246103.

(38) Ferrando, R.; Spadacini, R.; Tommei, G. E. Kramers Problem in Periodic Potentials: Jump Rate and Jump Lengths. *Phys. Rev. E* **1993**, *48* (4), 2437−2451.

(39) Ala-Nissila, T.; Ferrando, R.; Ying, S. C. Collective and Single Particle Diffusion on Surfaces. *Adv. Phys.* **2002**, *51* (3), 949−1078.

(40) Miret-Artés, S.; Pollak, E. The Dynamics of Activated Surface Diffusion. *J. Phys.: Condens. Matter* **2005**, *17* (49), S4133−S4150.

(41) Antczak, G.; Ehrlich, G. Jump Processes in Surface Diffusion. *Surf. Sci. Rep.* **2007**, *62* (2), 39−61.

(42) Fu, Q.; Wagner, T. Interaction of Nanostructured Metal Overlayers with Oxide Surfaces. *Surf. Sci. Rep.* **2007**, *62* (11), 431−498.

(43) Veit, R. D.; Farber, R. G.; Sitaraman, N. S.; Arias, T. A.; Sibener, S. J. Suppression of Nano-Hydride Growth on Nb(100) Due to Nitrogen Doping. *J. Chem. Phys.* **2020**, *152* (21), 214703.

(44) Dickey, J. M.; Strongin, M.; Kammerer, O. F. Studies of Thin Films of Nb$_3$Sn on Nb. *J. Appl. Phys.* **1971**, *42* (13), 5808−5820.

(45) Lee, J.; Posen, S.; Mao, Z.; Trenikhina, Y.; He, K.; Hall, D. L.; Liepe, M.; Seidman, D. N. Atomic-Scale Analyses of Nb$_3$Sn on Nb Prepared by Vapor Diffusion for Superconducting Radiofrequency Cavity Applications: A Correlative Study. *Supercond. Sci. Technol.* **2019**, *32* (2), No. 024001.

(46) Sayeed, M. N.; Pudasaini, U.; Reece, C. E.; Eremeev, G.; Elsayed-Ali, H. E. Structural and Superconducting Properties of

Nb₃Sn Films Grown by Multilayer Sequential Magnetron Sputtering. *J. Alloys Compd.* **2019**, *800*, 272−278.

(47) Strozier, J. A.; Miller, D. L.; Kammerer, O. F.; Strongin, M. Alloys of Sn and Ge on Nb Surfaces. *J. Appl. Phys.* **1976**, *47*, 1611.

(48) Bowman, A. L.; Wallace, T. C.; Yarnell, J. L.; Wenzel, R. G. The crystal structure of niobium monoxide. *Acta Crystallogr.* **1966**, *21*, 843.

(49) An, B.; Fukuyama, S.; Yokogawa, K.; Yoshimura, M. Surface Structures of Clean and Oxidized Nb(100) by LEED, AES, and STM. *Phys. Rev. B* **2003**, *68* (11), 115423.

📖 Recommended by ACS

C₆₀ Adsorbed on Ni(111) and Co(0001) Surfaces

Joseph A. Smerdon, Katariina Pussi, *et al.*

JANUARY 10, 2023
THE JOURNAL OF PHYSICAL CHEMISTRY C

READ 🗗

Two-Dimensional Ferroelectricity in a Single-Atom Adsorbed BiI₃ Monolayer

Zeying Zhou, Erjun Kan, *et al.*

FEBRUARY 10, 2023
THE JOURNAL OF PHYSICAL CHEMISTRY C

READ 🗗

Room-Temperature Preparation of Large-Area Transparent Two-Dimensional ZnO-Doped Ga₂O₃ Nanostructure-Based Layers: Implications for Optoelectronic Nanodevices

Qing Liu, Baodan Liu, *et al.*

FEBRUARY 08, 2023
ACS APPLIED NANO MATERIALS

READ 🗗

Performance, Emission, and Catalytic Activity Analysis of AL₂O₃ and CEO₂ Nano-Additives on Diesel Engines Using Mahua Biofuel for a Sustainable Environment

Abdul Zubar Hameed and Kandasamy Muralidharan

JANUARY 31, 2023
ACS OMEGA

READ 🗗

Get More Suggestions >